Experimental study of libration-driven zonal flows in a straight cylinder

J. Noir [a,*], M.A. Calkins [b], M. Lasbleis [c], J. Cantwell [a], J.M. Aurnou [a]

[a] Department of Earth and Space Sciences, University of California, Los Angeles, CA 90095-1567, USA
[b] Department of Mechanical and Aerospace Engineering, 48-121 Engineering IV, University of California, 420 Westwood Plaza, Los Angeles, CA 90095-1597, USA
[c] Ecole Normal Superieure de Lyon, 15 parvis RenŽ Descartes - BP 7000 69342 Lyon Cedex 07, France

ARTICLE INFO

ABSTRACT

Forced longitudinal librations are oscillatory perturbations of the rotation rate of a planet resulting from a gravitational coupling with orbital partners. In the present study we report the first experimental evidence that a librating cylindrical container can viscously drive mean azimuthal flows in the liquid interior, hereafter referred to as zonal flows. Using a novel laser Doppler velocimetry system, the current work extends upon the study of libration-driven flows by Noir et al. (2009). We investigate the different mechanisms underlying the zonal flow generation. It is found that zonal flows in the interior result primarily from non-linearities in the Ekman boundary layer. Furthermore, the zonal flow scales as the square of the libration amplitude and is independent of the Ekman number. This scaling implies that forced longitudinal libration in an axisymmetric container (purely viscous coupling) will drive unobservably small zonal flows at planetary conditions. Thus, purely viscous librational coupling will not generate significant energy dissipation in a planetary fluid layer. It follows that any observed phase lag between the gravitational forcing and the orbital response of a planet requires non-viscous coupling mechanisms to account for the energy dissipation.

Published by Elsevier B.V.

1. Introduction

Several planets in our solar system undergo forced longitudinal librations, a periodic oscillation of the axial rotation rate that results from gravitational interactions with an orbital partner (Yoder, 1995; Comstock and Bills, 2003). Many librating bodies are believed to possess an internal liquid layer either in the form of a subsurface ocean on Titan, Europa, Callisto, Ganymede and Enceladus or in the form of a partially molten iron core as for Mercury, Io and the Earth's moon (Anderson et al., 1996, 1998, 2001; Williams et al., 2001; Spohn and Schubert, 2003; Hauck et al., 2004; Margot et al., 2007; Breuer et al., 2007; Williams et al., 2007; Van Hoolst et al., 2008; Lorenz et al., 2008). It has been argued that an internal liquid layer in a planet will decouple the librating solid shell from the interior (Peale and Boss, 1977; Wu et al., 1997; Peale et al., 2002; Van Hoolst et al., 2008). Such an argument has been made to explain Mercury's large libration amplitude (Margot et al., 2007).

The librating shell and the liquid layer are coupled through various mechanisms, including topographic, gravitational, electromagnetic and viscous processes. Here we consider the viscous coupling that occurs in a perfectly axisymmetric container surrounding a homogeneous, non-conductive fluid. This will provide a basic model on which future studies can be built. Prior numer-

ical and experimental studies have shown that viscous coupling between the fluid and the librating shell can drive complex internal flows (Aldridge, 1967, 1975; Aldridge and Toomre, 1969; Tilgner, 1999; Noir et al., 2009). The accurate characterization of the flows is important to better understand the energy and angular momentum budgets and the magnetic field generation processes of librating planets. Furthermore, coupling high precision planetary orbital measurements to accurate models of mechanically driven flows will constrain models of internal planetary structure (e.g., Margot et al., 2007) and core–mantle interaction (e.g., Buffett, 1992; Jault, 2000; Holme and de Viron, 2005).

Numerical simulations (Tilgner, 1999; Noir et al., 2009) and laboratory experiments in a spherical geometry (Aldridge, 1967, 1975; Aldridge and Toomre, 1969; Noir et al., 2009) have revealed three regimes of flow driven by forced longitudinal libration. For small libration amplitudes the flow is dominated by inertial modes, the eigenmodes of an inviscid fluid enclosed in a rapidly rotating cavity (Greenspan, 1968). These purely oscillatory modes exist only for libration frequencies less than twice the rotation frequency. This limit corresponds to a transition of the Navier–Stokes equation from hyperbolic to elliptic. Resonance occurs when the libration frequency corresponds to the eigenfrequency of a particular mode (Aldridge and Toomre, 1969; Tilgner, 1999). At moderate libration amplitudes, centrifugal instabilities in the form of Taylor–Görtler vortices develop in the vicinity of the outer boundary near the equatorial region (Aldridge, 1967; Noir et al., 2009), while the interior remains dominated by inertial modes. Finally, for large enough

* Corresponding author. Tel.: +1 310 825 9296; fax: +1 310 825 2779.
  E-mail address: jerome@ess.ucla.edu (J. Noir).

libration amplitudes, boundary turbulence develops near the outer wall (Noir et al., 2009).

In the limit of low libration frequencies, Busse (2010) has shown that forced longitudinal libration in a spherical shell can drive a steady azimuthal (zonal) flow through non-linear interactions in the viscous (Ekman) boundary layer. The low frequency approximation allows Busse (2010) to derive an analytical solution, which predicts that the zonal flow scales with the square of the libration amplitude. This has been confirmed by the laboratory and numerical experiments of Sauret et al. (in press).

In the present paper, we consider a broad range of libration frequencies applicable to planetary conditions. We characterize the zonal flow driven in the liquid interior using the laboratory experimental setup of Noir et al. (2009), with a cylindrical cavity replacing the spherical shell used in the initial study. This allows us to test different source mechanisms of the zonal flow when inertial modes, centrifugal instabilities and Ekman layer non-linearities all coexist. The cylindrical geometry allows us to decouple, at first order, the horizontal Ekman boundary layers from the vertical Stewartson layer, in which Taylor–Görtler vortices develop. Our later analysis will be simplified by this decoupling.

The paper is organized as follows. Section 2 presents the governing equations and control parameters. The experimental setup is described in Section 3. The results are presented in Section 4. Section 5 is devoted to a discussion of possible source mechanisms for the zonal flow. Concluding remarks are presented in Section 6.

2. Governing equations and control parameters

Before discussing the laboratory setup, we present the basic equations and control parameters that describe our physical system.

Let us consider a cylindrical fluid cavity of outer cylindrical radius s_o and height h. The axis of revolution of the cylinder and the rotation axis are colinear and aligned along the $\hat{\boldsymbol{z}}$-direction. The origin of the cylindrical coordinate system (s, ϕ, z) is chosen to be at the center of the cavity. In the inertial reference frame, the instantaneous axial rate of rotation of the cylindrical container varies as

$$\Omega(t) = \Omega_0 + \Delta\phi\,\omega_L \sin(\omega_L t), \tag{1}$$

where Ω_0 is the mean rotation rate, $\Delta\phi$ is the amplitude of libration in radians and ω_L is the angular libration frequency. The fluid is assumed to be homogenous, incompressible and electrically non-conductive. In the reference frame rotating at Ω_0, the equations governing the motion of the fluid are

$$\frac{\partial \boldsymbol{u}}{\partial t} + \boldsymbol{u} \cdot \nabla\boldsymbol{u} + 2\Omega_0\hat{\boldsymbol{z}} \times \boldsymbol{u} = -\frac{1}{\rho}\nabla p + \nu\nabla^2\boldsymbol{u}, \tag{2}$$

$$\nabla \cdot \boldsymbol{u} = 0, \tag{3}$$

where $\boldsymbol{u}$ is the velocity; $\Omega_0\hat{\boldsymbol{z}}$ is the mean angular velocity vector; ρ denotes the constant fluid density; p is the modified pressure including the centrifugal term; and ν is the fluid's kinematic viscosity.

The fluid satisfies the sidewall boundary conditions

$$\begin{aligned} \hat{\phi} \cdot \boldsymbol{u}(s_o, z) &= s_o[(\Delta\phi\,\omega_L)\sin(\omega_L t)], \\ \hat{\boldsymbol{s}} \cdot \boldsymbol{u}(s_o, z) &= 0, \\ \hat{\boldsymbol{z}} \cdot \boldsymbol{u}(s_o, z) &= 0, \end{aligned} \tag{4}$$

as well as the top and bottom lid boundary conditions

$$\begin{aligned} \hat{\phi} \cdot \boldsymbol{u}(s, \pm h/2) &= s[(\Delta\phi\,\omega_L)\sin(\omega_L t)], \\ \hat{\boldsymbol{s}} \cdot \boldsymbol{u}(s, \pm h/2) &= 0, \\ \hat{\boldsymbol{z}} \cdot \boldsymbol{u}(s, \pm h/2) &= 0. \end{aligned} \tag{5}$$

Eqs. (2)–(5) are non-dimensionalized using Ω_0^{-1} and the radius, s_o, as the respective units of time and length. The non-dimensional form of the equations then becomes

$$\frac{\partial \boldsymbol{u}}{\partial t} + \boldsymbol{u} \cdot \nabla\boldsymbol{u} + 2\hat{\boldsymbol{z}} \times \boldsymbol{u} = -\nabla p + E\nabla^2\boldsymbol{u}; \tag{6}$$

$$\nabla \cdot \boldsymbol{u} = 0; \tag{7}$$

subject to

$$u_\phi(1, z) = \varepsilon \sin(ft), \qquad u_\phi(s, \pm\chi) = s\varepsilon \sin(ft). \tag{8}$$

Here $\chi = h/2s_o$ is the aspect ratio of the cylinder. Throughout the remainder of this paper, all quantities are non-dimensional unless otherwise noted. The Ekman number, E, measures the ratio of the viscous and the Coriolis forces:

$$E = \frac{\nu}{\Omega_0 s_o^2}. \tag{9}$$

In the present paper we consider the case of finite aspect ratio cylinders, $\chi \sim O(1)$. It follows that our definition of the Ekman number can be recast in terms of the more classical Ekman number, $E_o = \nu/(\Omega_0 h^2)$, as

$$E = 4E_o\chi^2. \tag{10}$$

The librational forcing parameter, ε, measures the relative strength of the librational forcing to the background solid body rotation:

$$\varepsilon = \Delta\phi f, \tag{11}$$

where

$$f = \frac{\omega_L}{\Omega_0} \tag{12}$$

is the ratio of the angular frequency of libration and the mean angular frequency of rotation.

Using the standard nomenclature for boundary layers in a cylinder (Barcilon, 1968), the horizontal viscous boundary layers at the top and bottom of the cylindrical cavity are referred to as Ekman layers and the viscous layers that develop along the sidewall are called Stewartson layers. Anticipating the role of the non-linear terms in the Stewartson layer, we introduce the sidewall boundary layer Reynolds numbers:

$$Re_{bl} = \frac{u\delta}{\nu}, \tag{13}$$

where we use the sidewall boundary layer thickness δ as the characteristic length scale and the peak equatorial velocity of the shell as the characteristic velocity scale. It has been established that the vertical sidewall boundary layer consists of a double-layer structure. A layer of thickness $\delta \sim s_o E^{1/4}$ accommodates the azimuthal velocity difference between the side wall and the fluid in the interior whereas the radial gradient of vertical velocity is accommodated in a layer of thickness $\delta \sim s_o E^{1/3}$ (Barcilon, 1968). Considering the $O(E^{1/4})$-Stewartson layer and the peak azimuthal velocity $u = \Delta\phi\,\omega_L s_o$, the boundary layer Reynolds number can be expressed as:

$$Re_{bl} = E^{1/4}\frac{\Delta\phi\,\omega_L s_o^2}{\nu} = \varepsilon E^{-3/4}. \tag{14}$$

This parameter measures the relative strength of the inertial and viscous forces in the $O(E^{1/4})$ Stewartson layer that accommodates the azimuthal velocity field.

Typical laboratory values of the physical and non-dimensional parameters are given in Table 1. (For a detailed list of planetary values see Table 2 of Noir et al., 2009.) Also shown in Table 1 are the eigenfrequencies, f_{nm0}, of the inviscid axisymmetric inertial modes in a straight cylinder of aspect ratio $\chi = 1.07$ with values closest to the libration frequencies used in the present study. We have

Table 1
Summary of dimensionless parameter sets used to investigate the zonal flow generation in a straight cylinder of aspect ratio $\chi = 1.07$. The inviscid eigenfrequencies f_{nm0} for axisymmetric inertial modes are calculated from Greenspan (1968).

E	ε	f	f_{nm0}
10^{-4}	0.4	1	$f_{110} = 1.04$
10^{-4}	0.8	1	$f_{110} = 1.04$
5×10^{-5}	0.4	1	$f_{110} = 1.04$
5×10^{-5}	0.8	1	$f_{110} = 1.04$
3×10^{-5}	0.4	1	$f_{110} = 1.04$
3×10^{-5}	0.8	1	$f_{110} = 1.04$
5×10^{-5}	0.8	0.5	$f_{130} = 0.51$
5×10^{-5}	0.8	2	$f_\infty = 2$
5×10^{-5}	0.8	3	–

Table 2
Physical and dimensionless parameter definitions and their typical values in the laboratory experiment.

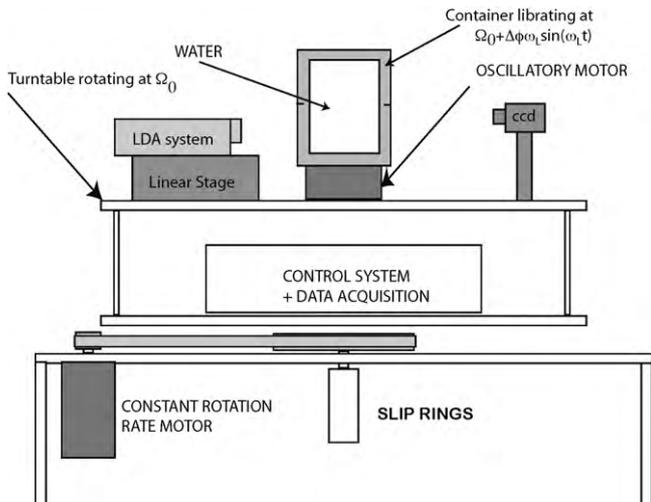| Parameter	Definition	Experiment
s_o	Outer boundary radius	88.9 mm
h	Cylinder height	190 mm
$\Omega_0/2\pi$	Mean rotation frequency	0.017–1 Hz
$\omega_L/2\pi$	Libration frequency	0.1–2 Hz
$\Delta\phi$	Angular displacement	$0-\pi$
ν	Kinematic viscosity	$10^{-6}\,\mathrm{m^2\,s^{-1}}$
E	$\nu/(\Omega_0 s_o^2)$	10^{-5} to 10^{-3}
f	ω_L/Ω_0	0.1–3
χ	$h/(2s_o)$	1.07
ε	$\Delta\phi f$	0–5
Re_{bl}	$\varepsilon E^{-3/4}$	$\lesssim 400$

calculated these inviscid eigenfrequencies using Eq. (2.15.7) from Greenspan (1968). At first order, the n and m indexes represent the radial and axial wave numbers, respectively. The limit case $f = 2$ corresponds to a mode of infinite axial wave number and is denoted here by f_∞.

3. Experimental set-up

3.1. Laboratory apparatus

Fig. 1 shows a schematic view of the laboratory device used in the present study. It is the same device used in Noir et al. (2009) with the exception of the container and the addition of a laser Doppler velocimeter (LDV) to measure the fluid velocity. A detailed description of the basic apparatus can be found in Noir et al. (2009). The oscillation of the acrylic container is directly driven by a ring-style servomotor. The container and the ring-servo are centered on the upper deck of a 1 m diameter turntable that simulates the mean rotation rate of the planet. The acrylic container consists of a right cylinder ($s_o = 88.9$ mm, $h = 190$ mm), which corresponds to an aspect ratio $\chi = 1.07$. The rotation frequency of the turntable can be set from 0.017 to 1 Hz (1–60 rpm, respectively) and is stable to better than $\pm 0.5\%$. The parameter values accessible with this device are given in Table 2.

Each libration experiment follows a standard protocol. First the turntable rotates for ~5 to 15 min to enable the fluid to spin-up to a state of solid body rotation. Then the ring-servo is activated to oscillate the acrylic container. Flow imaging and LDV measurements are then carried out.

Fig. 1. Schematic view of the laboratory experiment.

3.2. Diagnostic methods

In our experiments the working fluid is seeded with Kalliroscope flakes to visualize shear zones in the fluid (e.g., Noir et al., 2009). Boundary layer flow characterizations are carried out with high concentrations of Kalliroscope flakes, which make the fluid opaque except in the vicinity of the acrylic walls. Shear zones in the fluid interior are visualized using a 1/1000 solution of Kalliroscope. Still images and movies are made with cameras and light sources in the rotating frame.

We use the "ultraLDV" system developed by Measurement Scientific Enterprise to quantitatively measure the velocity inside the fluid cavity. This LDV system was designed specifically to make low velocity measurements in rapidly rotating environments, characterized by large centrifugal and gyroscopic forces. (Device details can be found at http://www.measurementsci.com.)

LDV measurements in container with curved walls require post-processing to account for the changes in fringe separation due to optical distortion and for changes in the wavelength of the laser light beams in the liquid. In addition, LDV time series usually exhibit non-uniform sampling frequencies, which affect subsequent statistical analyses. We present the LDV methodology in Appendix A.

The LDV is mounted on a computer-controlled linear stage. This allows us to acquire azimuthal velocity profiles along a cylindrical radius, hereafter referred to as radial profiles. Both the LDV system and the computer are in the rotating frame. Thus, we always measure the secondary flow relative to the background solid body rotation. Each radial profile consists of 70 points total. The points are spaced approximately 2 mm apart from $s \simeq 10$ mm to $s \simeq 82$ mm and are spaced 0.2 mm apart from $s \simeq 82$ mm to $s \simeq 89$ mm. We acquire time series of the azimuthal velocity over 20 periods of libration at each point. The time-averaged velocity and standard deviation of each time series are used to construct the mean zonal velocity profiles.

4. Results

4.1. Sidewall instabilities

Prior to zonal flow measurements, we use direct visualization to carry out a systematic exploration of the parameter space (E, ε) accessible with our laboratory experiment. We vary the Ekman number, E, by changing the rotation rate of the turntable. The librational forcing parameter, ε, can be adjusted by varying either the amplitude of the oscillation $\Delta\phi$ or by varying the frequency of libration ω_L.

Three flow regimes are observed. For weak librational forcing, the flow remains stable in the entire volume. Above some critical forcing, ε_c, the sidewall boundary layer undergoes centrifugal
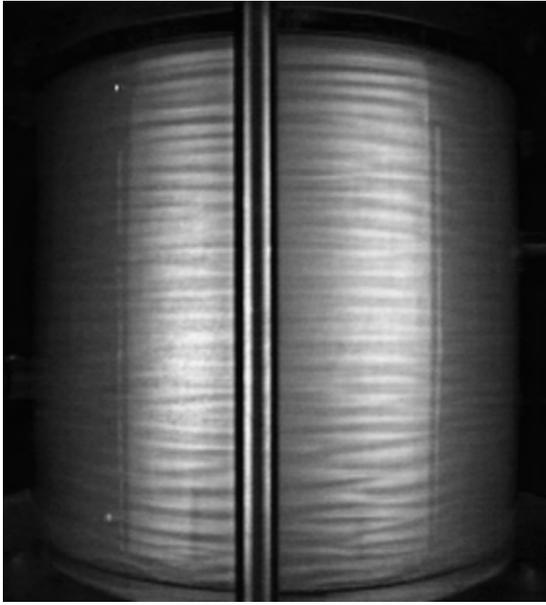
Fig. 2. Taylor–Görtler vortices along the sidewall at the end of the retrograde phase ($\Omega = \Omega_0 - \Delta\phi\omega_L$). The control parameters in this case are $\varepsilon = 0.35$ and $E = 5 \times 10^{-5}$. The vertical bar in the center in the image is an aluminum tie rod that connects device's top and bottom lids.

Fig. 3. Compiled experimental results from direct visualization plotted in terms of the libration forcing ε versus the Ekman number E. Flow regimes: stable boundary layer ($\bigcirc$); boundary layer instability ($\bullet$); constant boundary layer Reynolds, $Re_{bl} = 250$ (solid black line).

instabilities in the form of Taylor–Görtler vortices (e.g., Saric, 1994) that are confined to the outermost region of the fluid (see Fig. 2). For large enough ε, the Taylor–Görtler vortices become wavy and eventually turbulent. No clear transition has been found between the Taylor–Görtler vortices, the wavy Taylor–Görtler vortices and the boundary turbulence. Thus, we consider all three to define the unstable regime. The Taylor–Görtler vortices form primarily during the portion of the libration cycle when the shell moves in the opposite direction to the turntable (retrograde phase) and dissipate during the rest of the cycle (prograde phase). Similar observations in spherical shell geometries have been reported by Aldridge (1967) and Noir et al. (2009).

In the straight cylinder used in the present study, the Taylor–Görtler vortices and the boundary turbulence appears at nearly the same time everywhere along the sidewall, as shown in Fig. 2. As a consequence, we expect any effects of side wall instabilities on the interior flow to be enhanced in a straight cylinder. In contrast, in a spherical cavity, these instabilities tend to form near the equatorial region and travel toward the poles due to the advection from the Ekman pumping (Aldridge, 1967; Noir et al., 2009; Calkins et al., in press). However, at planetary settings ($E \lesssim 10^{-10}$), the Ekman pumping, which is proportional to $E^{1/2}$ is expected to be negligible. Thus, the boundary layer instabilities will tend to remain confined to the equatorial region in a spherical shell at planetary conditions (Calkins et al., in press).

Fig. 3 represents a compilation of our observations in an (E, ε) parameter space. The transition from the stable to unstable regime is well characterized by a constant boundary layer Reynolds number based on the thickness of the sidewall Stewartson layer, Re_{bl}. This critical boundary layer Reynolds number, Re_{bl}^*, represents the limit above which the adverse gradient of angular momentum overcomes viscous damping in the boundary layer. We performed a linear regression on the data points on each side of the transition in Fig. 3 to determine the critical value of the boundary layer Reynolds number. We obtain $Re_{bl}^* = 250 \pm 5$, where the mean value is shown in Fig. 3. This result can be recast in terms of a critical librational forcing parameter ε_c:
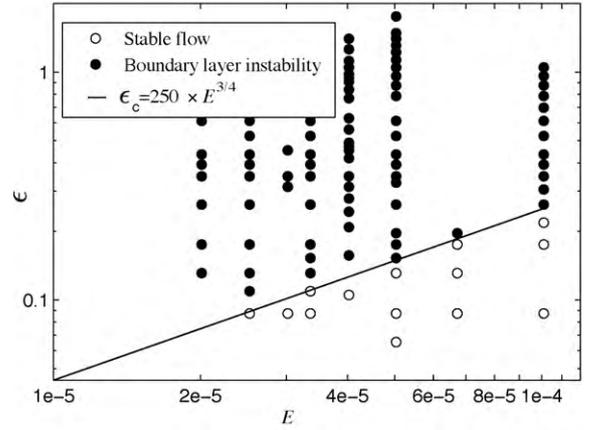
$$\varepsilon_c = Re_{bl}^* E^{3/4} \qquad (15)$$

Further discussions of centrifugal instabilities in librating systems can be found in Noir et al. (2009) and Calkins et al. (in press).

4.2. Libration-driven zonal flows

Radial profiles of azimuthal velocity have been acquired for the 9 different parameter sets presented in Table 1. Fig. 4 shows the six zonal velocity profiles at $f = 1$. Fig. 4a and c corresponds to physical quantities; Fig. 4b and d represents the same data plotted in terms of the dimensionless quantities. In the six profiles presented here, the libration frequency is equal to the rotation frequency, $f = 1$. In these cases, the librational forcing parameter, ε, reduces to the amplitude of libration. The first and second rows in Fig. 4 correspond, respectively, to $\varepsilon = 0.4$ ($\Delta\phi \approx \pi/8$) and $\varepsilon = 0.8$ ($\Delta\phi \approx \pi/4$). In each plot we present the velocity profiles for three values of the Ekman number $E = 10^{-4}$, $E = 5 \times 10^{-5}$ and $E = 3 \times 10^{-5}$, which correspond, respectively, to $\Omega_0 = 14$ rpm, $\Omega_0 = 24$ rpm and $\Omega_0 = 40$ rpm. All of our experiments are carried out in the unstable regime. (LDV measurements were not possible in the stable regime due to the small velocities generated at low ε.) For $E = 10^{-4}$ and $E = 5 \times 10^{-5}$, both $\varepsilon = 0.4$ and $\varepsilon = 0.8$ correspond to cases with nearly axisymmetric Taylor–Görtler vortices forming near the sidewall. In contrast, for $E = 3 \times 10^{-5}$ and $\varepsilon = 0.8$, boundary turbulence develops during the retrograde phase of the libration cycle.

In all our experiments, we observe a retrograde flow that is characterized by a nearly solid body rotation in the bulk of the fluid ($s \lesssim 0.7$). Between $0.9 \lesssim s \lesssim 0.98$, a strong retrograde jet develops, as seen in Fig. 4. In addition, we measure a prograde flow adjacent to the sidewall. From Fig. 4b and d, it appears that the zonal flow profiles converge with decreasing values of E.

Fig. 5a presents radial profiles of dimensionless velocities normalized by ε^2 for the $f = 1$ cases presented in Table 1. At first order, the various profiles collapse onto the same curve for $s \lesssim 0.9$. The results of Figs. 4b, d and 5a suggest that, at low E, an asymptotic regime exists where the $f = 1$ zonal flow in the interior ($s \lesssim 0.9$) is independent of Ekman and scales as ε^2. Similar results are reported in the numerical study in a spherical shell by Calkins et al. (in press).

The zonal flows we observe may be influenced by the dynamics of inertial modes at $f \leq 2$. To investigate this possibility, we have carried out complementary experiments at $E = 5 \times 10^{-5}$, $\varepsilon = 0.8$ and $f = 0.5, 2$ and 3 (see Table 1). Indeed, at different frequencies, different inertial modes are excited, which may contribute to the zonal flow. If so, we expect a different signature of the inertial mode contribution to the zonal flow at $f = 0.5, 1$ and 2. For each f in the present
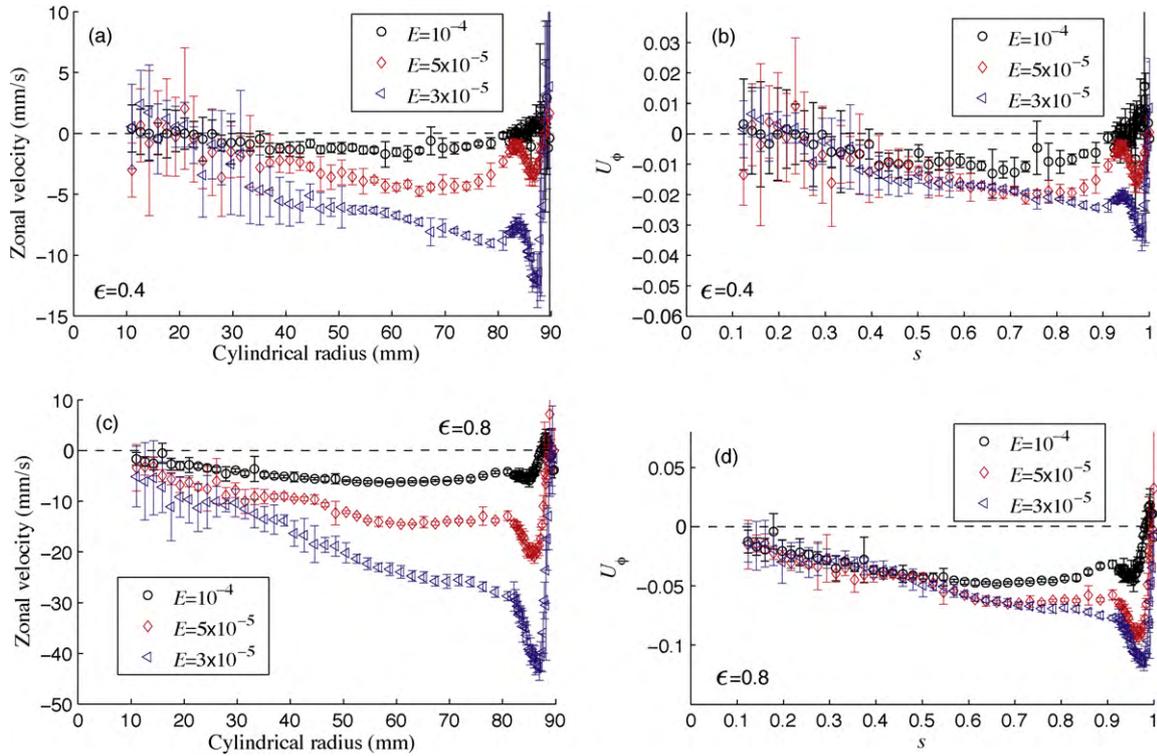
Fig. 4. Zonal velocity profiles at $f=1$ along a cylindrical radius located 2 cm above the mid-plane. All measurements are performed in the boundary layer instability regime. (a) and (c) Physical quantities, (b) and (d) Dimensionless quantities. Top and bottom rows corresponds to $\varepsilon = 0.4$ and $\varepsilon = 0.8$, respectively.
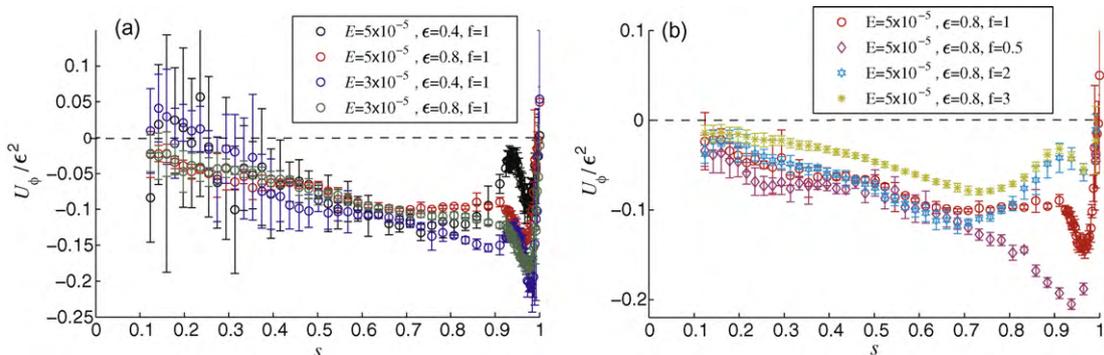
paper, the closest inviscid eigenfrequencies and their associated inertial modes are reported in Table 1.

Fig. 5b presents profiles of zonal velocity normalized by ε^2. For $f \leq 2$ and $s \lesssim 0.7$, we do not observe any significant variation of the normalized zonal velocity. For $f \leq 2$ and $s \gtrsim 0.7$, the radial profiles differ both in shape and amplitude.

For the $f=3$ case, inertial modes cannot develop in the fluid interior (e.g., Greenspan, 1968). Yet the $f=3$ zonal velocity profile qualitatively agrees with all other data sets. In detail, we note a slight decrease of the amplitude of the zonal velocity in that case.

We have measured time series of the zonal velocity at a fixed location to determine the typical time scale for the zonal flow to equilibrate after the oscillation of the cylinder is initiated. Fig. 6 shows a time series of the dimensionless velocity $u_\phi(t)$ at $s=0.55$, which illustrates the typical growth of the zonal flow. Time is normalized by the spin-up time scale t_Ω, which is defined as

$$t_\Omega = 2\chi E^{-1/2} \Omega_0^{-1}. \tag{16}$$

The oscillation of the cylinder starts at $t/t_\Omega = 0$. In all our experiments, the system equilibrates within roughly one spin-up time, $t/t_\Omega \sim 1$. This result holds even for the $f=3$ case, where no inertial modes develop.

5. Zonal flow mechanisms

From our experiments, we infer that the time-averaged zonal velocity U_ϕ is independent of E and scales as ε^2 in the inner region of the fluid, $s \lesssim 0.9$. In addition, the zonal flow equilibrates within a spin-up time from the start of the oscillation of the cylindrical cavity. We have isolated three possible mechanisms that can lead to zonal flow generation. These three mechanisms are Reynolds stresses interactions of inertial modes in the interior, Reynolds stresses due to oscillatory pumping in the Ekman layers and Reynolds stresses due to the sidewall boundary instabilities. The Taylor–Görtler vortices form mainly during the retrograde phase of the cycle. Thus, they will typically advect low angular

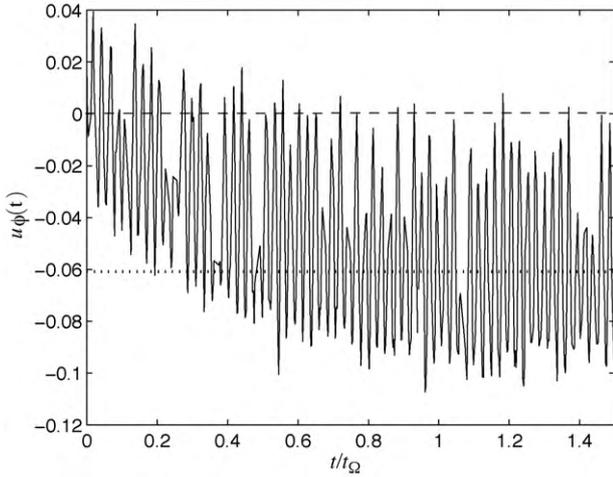
Fig. 5. (a) Non-dimensional radial profiles of zonal velocities normalized by ε^2 for the parameter sets in Table 1 at $f=1$. (b) Non-dimensional zonal velocity radial profile at $E = 5 \times 10^{-5}$, $\varepsilon = 0.8$ and $f = 0.5, 1, 2, 3$. Note that above $f=2$ inertial modes cannot develop in the system.

Fig. 6. Time series of the dimensionless velocity $u_\phi(t)$ at $s = 0.55$ ($E = 5 \times 10^{-5}$, $\varepsilon = 1$, $f = 1$) showing the development of the zonal flow upon initiation of libration. The oscillation of the outer cylindrical shell starts at $t/t_\Omega = 0$, where $t_\Omega = 2\chi E^{-1/2} \Omega_0^{-1}$ is the spin-up time scale. The dotted line represents the time average zonal velocity after the flow reaches a statistically steady state.

momentum fluid from the Stewartson layer into the interior region next to the sidewall. This angular momentum will then diffuse viscously inward. However, viscous diffusion phenomena arise on a timescale $t_\nu = s_0^2/\nu$, which using the definition of the Ekman number (9) can be recast as $t_\nu = E^{-1}\Omega_0^{-1}$. In contrast, we observe that the zonal flow equilibrates within a much shorter timescale, typically of the order of a spin-up time, $t_\Omega = 2\chi E^{-1/2}\Omega_0^{-1}$. It is therefore unlikely that the Taylor–Görtler vortices are responsible for the steady zonal flow in the interior of the cavity. However, they may influence the zonal flow in the region adjacent to the sidewall, where we report retrograde and prograde peaks of zonal velocity.

Here we consider the two other possible source mechanisms. To determine the order of magnitude of the zonal flow, we will scale the time-averaged torque balance on a straight cylindrical surface $\Sigma(s)$ that extends from the bottom to the top solid surfaces. This surface is referred to as a geostrophic cylinder.

The flow and pressure fields are decomposed into steady components, ($\boldsymbol{U}$, P), and time dependent components, ($\mathbf{u(t)}$, $p(t)$). The time-averaged Navier–Stokes equations then becomes:

$$2\hat{\boldsymbol{z}} \times \boldsymbol{U} + \overline{\boldsymbol{u} \cdot \nabla \boldsymbol{u}} = -\nabla P + E\nabla^2 U. \quad (17)$$

The time-averaged axial torque on a geostrophic cylinder is obtained by integrating ($\hat{z} \cdot (\boldsymbol{s} \times (17))$) on Σ:

$$0 = -2s^2 \iint_\Sigma U_s \, d\phi dz - s^2 \iint_\Sigma \overline{\boldsymbol{u} \cdot \nabla \boldsymbol{u}} \cdot \hat{\phi} \, d\phi dz$$
$$-s^2 \iint_\Sigma \frac{\partial P}{\partial \phi} \, d\phi dz + s^2 E \iint_\Sigma \nabla^2 U_\phi \, d\phi dz. \quad (18)$$

Using the non-penetration condition at the top and bottom solid surfaces, $\boldsymbol{U} \cdot \hat{\boldsymbol{z}} = 0$, mass conservation leads to:

$$\iint_\Sigma U_s \, d\phi dz = 0. \quad (19)$$

This demonstrates that the torque due to the Coriolis force, the first term on the right hand side of (18), is identically zero. In addition, the integration of the pressure gradient over 2π radians in ϕ is also identically zero. It follows that (18) reduces to:

$$0 = -\iint_\Sigma \overline{\boldsymbol{u} \cdot \nabla \boldsymbol{u}} \cdot \hat{\phi} \, d\phi dz + E \iint_\Sigma \nabla^2 U_\phi \, d\phi dz. \quad (20)$$

For small E, the viscous forces are important only in the Ekman boundary layers. Thus, the time-averaged viscous torques in (20) vanish in the interior; the integration can be performed only over the portion of Σ in the top and bottom Ekman boundary layers. Assuming the flow is symmetric with respect to the mid-plane of the cylinder, both the top and bottom boundary layers will contribute equally to the viscous torque, which allows us to integrate only over the top Ekman layer. Since the zonal flow is axisymmetric, the viscous torque in (20) reduces to:

$$E \iint_\Sigma \nabla^2 U_\phi \, d\phi dz = 2E \int_0^{2\pi} d\phi \int_0^{E^{1/2}} \nabla^2 U_\phi \, dz. \quad (21)$$

In the boundary layer $(\partial^2/\partial z^2) \sim O(E^{-1})$ and $(\partial^2/\partial s^2) \sim O(1)$. Integrating in ϕ and neglecting the radial derivatives yields:

$$E \iint_\Sigma \nabla^2 U_\phi \, d\phi dz = 4\pi E \int_0^{E^{1/2}} \frac{\partial^2 U_\phi}{\partial z^2} \, dz. \quad (22)$$

It follows that the viscous torque in the boundary layer is of order:

$$E \iint_\Sigma \nabla^2 U_\phi \, d\phi dz \sim 4\pi E^{1/2} U_\phi. \quad (23)$$

In order to estimate the non-linear term in (20), we separately consider the contributions from the boundary layer and from the interior. The non-linear torque in the boundary layer is

$$2 \int_0^{2\pi} d\phi \int_0^{E^{1/2}} \overline{\boldsymbol{u} \cdot \nabla \boldsymbol{u}} \cdot \hat{\phi} \, dz = 4\pi \int_0^{E^{1/2}} \left(\overline{u_z \frac{\partial u_\phi}{\partial z}} + \overline{u_s \frac{\partial u_\phi}{\partial s}} \right) dz. (24)$$

The flow in the Ekman boundary layers is assumed to be qualitatively similar to that resulting from an impulsive spin-up (spindown) during the prograde (retrograde) phase. For the purposes of this estimate, we use the linear solution for flow in the boundary layers. From Greenspan (1968), we retain the typical amplitude of the flow in the boundary layer and its radial dependency away from the sidewall:

$$\begin{aligned} u_s &\sim s\varepsilon, \\ u_\phi &\sim s\varepsilon, \\ u_z &\sim \varepsilon E^{1/2}. \end{aligned} \quad (25)$$

During the prograde phase, similar to the case of an impulsive spin-up, the Ekman circulation pumps fluid from the interior into the top boundary layer, $u_z > 0$. Since the azimuthal velocity during spin-up is positive and increases with z, we find:

$$u_z \frac{\partial u_\phi}{\partial z} > 0. \quad (26)$$

Since the spin-up azimuthal velocity increases linearly with s, it follows that $(\partial u_\phi/\partial s) > 0$. In addition, the spin-up radial velocity is pointing outward, $u_s > 0$. Thus, during the prograde phase of libration:

$$u_s \frac{\partial u_\phi}{\partial s} > 0. \quad (27)$$

During the retrograde phase, similar to the case of a linear impulsive spindown, all velocities have an opposite sign. This implies that the non-linear terms are also positive during the retrograde phase. Then from (25), we have

$$\overline{u_z \frac{\partial u_\phi}{\partial z}} + \overline{u_s \frac{\partial u_\phi}{\partial s}} \sim s\varepsilon^2, \quad (28)$$

and the non-linear torque in the boundary layer scales as

$$2 \int_0^{2\pi} d\phi \int_0^{E^{1/2}} \overline{\boldsymbol{u} \cdot \nabla \boldsymbol{u}} \cdot \hat{\phi} \, dz \sim 4\pi E^{1/2} s\varepsilon^2. \quad (29)$$

The interior torque acting on the geostrophic cylinder Σ is

$$2 \int_0^{2\pi} d\phi \int_0^{(\chi - E^{1/2})} \overline{\boldsymbol{u} \cdot \nabla \boldsymbol{u}} \cdot \hat{\phi} \, dz$$

$$= 4\pi \int_0^{(\chi - E^{1/2})} \left(\overline{u_z \frac{\partial u_\phi}{\partial z}} + \overline{u_s \frac{\partial u_\phi}{\partial s}} \right) dz. \tag{30}$$

In contrast with the boundary layer, the typical length scale in the interior is $O(1)$. Assuming the interior flow velocities are $O(\varepsilon E^{1/2})$ (Greenspan, 1968), it follows that

$$\overline{u_z \frac{\partial u_\phi}{\partial z}} + \overline{u_s \frac{\partial u_\phi}{\partial s}} \sim E\varepsilon^2. \tag{31}$$

It follows from (30) that

$$2 \int_0^{2\pi} d\phi \int_0^{(\chi - E^{1/2})} \overline{\boldsymbol{u} \cdot \nabla \boldsymbol{u}} \cdot \hat{\phi} \, dz \sim 2\pi \chi E\varepsilon^2, \tag{32}$$

where we have assumed $E^{1/2} \ll \chi$. Thus, the torque produced by non-linearities in the interior is $E^{1/2}$ smaller than its boundary layer counterpart (29) and can therefore be neglected. It follows that the non-linear term in (20) scales as

$$\iint_\Sigma \overline{\boldsymbol{u} \cdot \nabla \boldsymbol{u}} \cdot \hat{\phi} \, d\phi dz \sim 4\pi E^{1/2} s\varepsilon^2. \tag{33}$$

Substituting (23) and (33) back into (20), we conclude that the interior zonal flow should scale as

$$U_\phi \sim s\varepsilon^2, \tag{34}$$

and is driven by non-linearities in the Ekman boundary layers. This heuristic scaling argument fails in describing the structure of the zonal flow profile in the outermost region of the fluid ($s \gtrsim 0.9$).

Our zonal flow scaling (34) is in agreement with the axisymmetric numerical study in a spherical shell of Calkins et al. (in press) and Busse's (2010) analytical solution in the limit of low libration frequency. In contrast with Busse (2010) and Sauret et al. (in press), we carry out our experiments in a range of frequencies for which inertial modes develop in the fluid. At the moderate Ekman numbers accessible with the present device, the inertial modes do not appear to significantly contribute to the zonal flow generation.

We conclude that Taylor–Görtler vortices and boundary turbulence do not contribute significantly to the zonal flow in the inner region of the fluid, $s \lesssim 0.9$. Boundary layer instabilities may have an effect in the vicinity of the sidewall where large retrograde and prograde peaks of the zonal velocity have been reported. In a spherical geometry, the boundary layer instabilities tend to be trapped in the equatorial region at low Ekman number (Calkins et al., in press; Noir et al., 2009). The effect of boundary instabilities on the interior zonal flow is expected to be further reduced in a spherical geometry at planetary settings.

6. Summary

We have reported the first experimental evidence that forced longitudinal libration can drive a net zonal flow in the fluid interior. LDV measurements of the time-averaged zonal velocity suggest that the amplitude of the zonal flow scales as $U_\phi \propto s\varepsilon^2$. Using heuristic arguments, we show that the retrograde zonal flow is driven by non-linear Ekman pumping in the top and bottom boundary layers. In addition, the contribution from the inertial modes in the interior and the boundary instabilities have been shown to be negligible in the range of parameters accessible with our apparatus.

In planetary settings, libration will lead to a coupling between the fluid interior and the surrounding shells. In general this coupling can consist of topographic, electromagnetic, gravitational and viscous components. In the present study we consider purely viscous coupling between an axisymmetric container and the liquid interior. Assuming (34) remains valid at planetary settings, we estimate the typical amplitude of the retrograde angular velocity generated in the liquid shell will be of the order of $10^{-8}\Omega_0$ for Mercury, Titan, Europa, Io, Callisto, Enceladus and the Earth's moon. Thus, viscously driven flows will not produce measurable variations in MESSENGER magnetic field data. Furthermore, purely viscous librational coupling will not generate significant energy dissipation in the fluid layer. Thus, any observed phase lag between the gravitational forcing and the orbital response of a planet requires non-viscous coupling mechanisms to account for the energy dissipation.

Acknowledgements

Appendix A. LDV methodology

In a laser Doppler velocimeter (LDV), a single laser beam is split into two identical beams, which are then refocussed at the location of measurement in the fluid, called the probe volume. A fringe pattern results from the interference of the split beams in the probe volume. We use titanium oxide (TiO_2) particles suspended in the fluid to act as optical scatterers. When the particles traverse the fringe pattern the scattered light intensity, measured by a photomultiplier, fluctuates. The frequency of the fluctuation equals the fluid velocity perpendicular to the fringe pattern divided by the fringe spacing. The absolute value of the velocity can then be expressed as:

$$|u| = F_D \Delta. \tag{35}$$

The fringe separation Δ depends on the wavelength of the laser beam and the laser beam splitting angle in the probe volume as:

$$\Delta = \frac{\lambda}{2 \sin \alpha}. \tag{36}$$

The manufacturer has calibrated Δ in air; we refer to this value as Δ_0. In general, the fringes separation in the fluid differs from its value in the air due to the changes in wavelength with the index of refraction and geometry of the laser light beam.

In order to determine uniquely the sign of the measured velocity it is necessary to introduce a phase lag between the two beams. In the ultraLDV the phase lag is achieved via two Bragg cells. This results in a fringe pattern that continuously travels in one direction, $\hat{k}_s$, through the probe volume. Thus, in the absence of motion the fringes moving across particles at rest will produce a signal at a frequency F_s, called the shifting frequency. Particles moving in the same direction as the fringe pattern will produce a signal of frequency $F_D < F_s$; particles moving in the opposite direction will produce a signal of frequency $F_D < F_s$. The velocity is then given by:

$$\boldsymbol{u} = (F_s - F_D)\Delta \hat{k}_s. \tag{37}$$

Let us define the index of refraction of air to be $n_0 = 1$, the laser light's wavelength in air to be $\lambda_0 = 658$ nm and the beam splitting angle in air to be $\alpha_0 = 7.9°$. We take $n_1 = 1.49$, λ_1 and α_1 for acrylic. Lastly, we take $n = 2 = 1.33$, λ_2 and α_2 for water. In the probe volume, the fringes separation is

$$\Delta_2 = \frac{\lambda_2}{2 \sin \alpha_2} \tag{38}$$
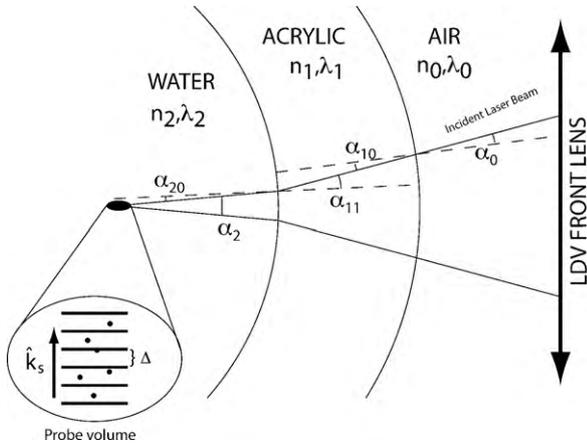
Fig. 7. Schematic view of the LDV laser light beams propagating through a curved wall.

where $\sin \alpha_2$ depends on the path of the laser light in the system and λ_2 is a function of the local index of refraction. This is given by

$$\lambda_2 = \frac{c}{n_2 f_o}, \tag{39}$$

where c is the speed of light in vacuum and f_o is the frequency of the laser light, which is invariant. At ambient pressure, $n_0 \simeq 1$, which yields $\lambda_0 = (c/f_o)$. In water the wavelength of the laser light is $\lambda_2 = 495$ nm. In order to calculate the correct velocity from the frequency of the backscattered light intensity it is necessary to evaluate $\sin \alpha_2$. We have developed a forward propagation model, illustrated in Fig. 7, which calculates the location of the probe volume and the splitting angle of the laser beams in the fluid. We use Snell–Descarte's law of refraction across the air-acrylic interface,

$$n_0 \sin \alpha_0 = n_1 \sin \alpha_{10}, \tag{40}$$

and the acrylic-water interface,

$$n_1 \sin \alpha_{11} = n_2 \sin \alpha_{20}, \tag{41}$$

to track the ray path through the system. In general, the geometrical relationship between α_{10} and α_{11}, α_{20} and α_2 is a function of the shape and of the thickness of the walls.

In all of our experiments we set the LDV device to measure the azimuthal component of velocity $U_\phi(s)$ by aligning the optical axis of the system in the cylindrical radius direction and orienting the plane containing the two laser beams parallel to the equator of the cylinder. In order to acquire radial velocity profiles $U_\phi(s)$, the LDV device is moved along the radial direction using a linear stage. We carry out our forward propagation model of the laser beams for each position of the LDV on the linear stage to determine $\sin \alpha_2$ and the location of the probe volume inside the fluid volume. We then calculate the fringe separation at each measurement point using (38). Finally, we apply (37) to determine the local velocity. Each radial profile consists of $U_\phi(s)$ measurements at N locations. Each U_ϕ value represents the averaging of time series acquired over 20 periods of libration at each location. For each time series, we apply a signal-to-noise ratio filter to remove noise peaks that may have been interpreted as velocity signal by the LDV processing algorithm. In addition, the LDV acquisition process is subject to some quality criteria. Therefore, the data sets are not typically spaced equally in time. This can lead to erroneous time averaging. To remedy this, the data is linearly resampled at 50 Hz prior to statistical processing.

Our LDV processing algorithm has been validated using zonal velocity profiles acquired with the main turntable at rest, while using the ring-servo to rotate the tank counterclockwise at $\Omega_0 = 0.16$ Hz (10 rpm) past the stationary LDV. After several spin-up
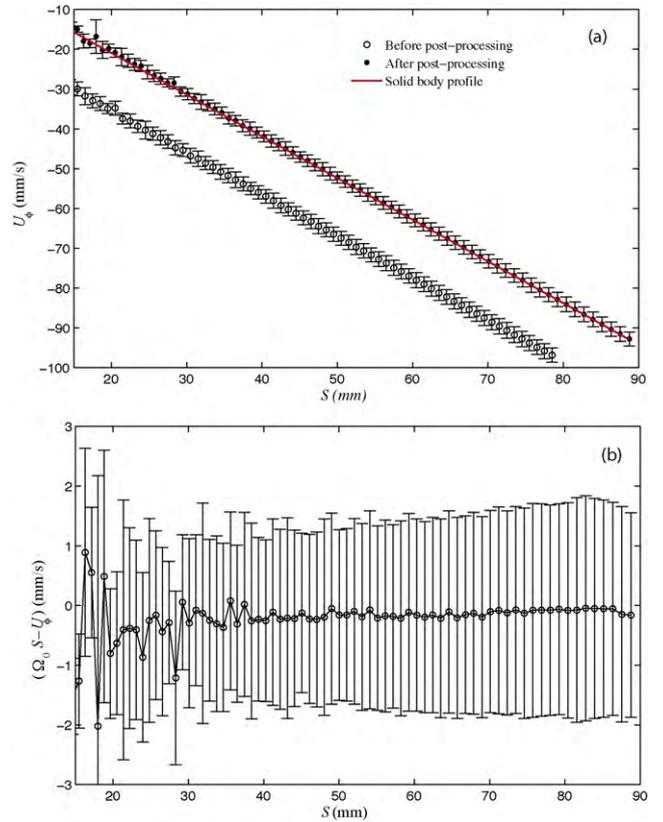
Fig. 8. Zonal velocity profiles along a cylindrical radius located 2 cm above the equatorial plan for a basic flow field of solid body rotation in a counter clockwise direction at $\Omega = 0.16$ Hz (10 rpm). (a) ($\bigcirc$) Velocity prior to LDV data post-processing; ($\bullet$) velocity from post-processed LDV data (red solid line) theoretical velocity profile of solid body rotation. (b) Difference between the theoretical profile and the post-processed LDV data. Error bars are defined in the text. (For interpretation of the references to color in this figure legend, the reader is referred to the web version of the article.)

time scales, the fluid velocity equilibrates to solid body rotation, $u_\phi = \Omega_0 s$. In Fig. 8a we present velocity profiles from this test. The raw output velocity profiles prior to fringe separation correction and signal processing are denoted by circles ($\bigcirc$), the post-processed velocity profile are denoted by bullets ($\bullet$) and the theoretical velocity profile for a solid body rotation at $\Omega_0 = 0.16$ Hz is denoted by the solid red line. The raw velocities calculated using the value of the fringe separation in air appear shifted toward larger values compare to the theoretical values. In contrast, the post-processed velocity profile accounting for the change in fringe separation is in very good agreement with the theoretical profile. Fig. 8b represents the departure of the post-processed LDV measurement from the theoretical profile. The error bars, which represents the fluctuations around the time-averaged value of U_ϕ, are comparable to the absolute resolution of the LDV system (2 mm/s). This test successfully validates our post-processing algorithm within the intrinsic resolution of the ultraLDV system.

We encountered three limitations during velocity profiles acquisition. First, LDV measurements within $\sim$2 mm from the sidewall are extremely difficult to carry out. Due to secondary modes created by the Bragg cell, secondary interference fringes form in the focal plane. As the probe volume approaches the sidewall, the secondary probe volume enters the acrylic shell. The interaction of the secondary probe volume and the moving shell produces a coherent signal of amplitude similar to or larger than the fluid signal. Both signals are at the same frequency and only slightly out of phase. Separating the two is usually not possible. Thus, the data in this region are not accurate and have large measurement uncertainties.

The second limitation of our system arises from low signal-to-noise ratio we measure when the probe volume is located deep inside the fluid. This occurs due to absorption and diffraction of light in the working fluid. This low SNR problem affects the data at $s \lesssim 35$ mm. Third, the ultraLDV's 17 cm focal length (in air) precludes measurement close to the container's rotation axis, at $s \lesssim 10$ mm.

References

Aldridge, K.D., 1967. An experimental study of axisymmetric inertial oscillations of a rotating liquid sphere. Ph.D. Thesis. Massachusetts Institute of Technology.

Aldridge, K.D., 1975. Inertial waves and earth's outer core. Geophysical Journal of the Royal Astronomical Society 42 (2), 337–345.

Aldridge, K.D., Toomre, A., 1969. Axisymmetric inertial oscillations of a fluid in a rotating spherical container. Journal of Fluid Mechanics 37, 307–323.

Anderson, J.D., Jacobson, R.A., McElrath, T.P., Moore, W.B., Schubert, G., Thomas, P.C., 2001. Shape, mean radius, gravity field, and interior structure of Callisto. Icarus 153 (1), 157–161.

Anderson, J.D., Lau, E.L., Sjogren, W.L., Schubert, G., Moore, W.B., 1996. Gravitational constraints on the internal structure of Ganymede. Nature 384 (6609), 541–543.

Anderson, J.D., Schubert, G., Jacobson, R.A., Lau, E.L., Moore, W.B., Sjogren, W.L., 1998. Europa's differentiated internal structure: inferences from four Galileo encounters. Science 281 (5385), 2019–2022.

Barcilon, V., 1968. Axi-symmetric inertial oscillations of a rotating ring of fluid. Mathematika 15, 93–102.

Breuer, D., Hauck, S.A., Buske, M., Pauer, M., Spohn, T., 2007. Interior evolution of mercury. Space Science Reviews 132 (2–4), 229–260.

Buffett, B.A., 1992. Constraints on magnetic energy and mantle conductivity from the forced nutations of the earth. Journal of Geophysical Review 97, 19581–19597.

Busse, F.H., 2010. Mean zonal flows generated by librations of a rotating spherical cavity. Journal of Fluid Mechanics 650, 505–512.

Calkins, M.A., Noir, J., Eldredge, J.D., Aurnou, J.M., in press. Axisymmetric simulations of libration-driven fluid dynamics in a spherical shell geometry. Phys. Fluids.

Comstock, R.L., Bills, B.G., 2003. A solar system survey of forced librations in longitude. Journal of Geophysical Research-Planets 108 (E9), 1–13.

Greenspan, H.P., 1968. The Theory of Rotating Fluids. Cambridge University Press, Cambridge.

Hauck, S.A., Dombard, A.J., Phillips, R.J., Solomon, S.C., 2004. Internal and tectonic evolution of mercury. Earth and Planetary Science Letters 222 (3–4), 713–728.

Holme, R., de Viron, O., 2005. Geomagnetic jerks and a high-resolution length-of-day profile for core studies. Geophysical Journal International 160, 435–439.

Jault, D., 2000. Earth's Core and Lower Mantle, Chapter 3: Electromagnetic and Topographic Coupling, and LOD Variations. Taylor and Francis, London.

Lorenz, R.D., Stiles, B.W., Kirk, R.L., Allison, M.D., Del Marmo, P.P., Iess, L., Lunine, J.I., Ostro, S.J., Hensley, S., 2008. Titan's rotation reveals an internal ocean and changing zonal winds. Science 319 (5870), 1649–1651.

Margot, J.L., Peale, S.J., Jurgens, R.F., Slade, M.A., Holin, I.V., 2007. Large longitude libration of mercury reveals a molten core. Science 316 (5825), 710–714.

Noir, J., Hemmerlin, F., Wicht, J., Baca, S., Aurnou, J., 2009. An experimental and numerical study of librationally driven flow in planetary cores and subsurface oceans. Physics of the Earth and Planetary Interiors 173, 141–152.

Peale, S.J., Boss, A.P., 1977. A spin–orbit constraint on the viscosity of a mercurian liquid core. Journal of Geophysical Research 82 (5), 743–749.

Peale, S.J., Phillips, R.J., Solomon, S.C., Smith, D.E., Zuber, M.T., 2002. A procedure for determining the nature of mercury's core. Meteoritics and Planetary Science 37 (9), 1269–1283.

Saric, W.S., 1994. Goërtler vortices. Annual Review of Fluid Mechanics 26, 379–409.

Sauret, A., Cebron, D., Morize, C., Le Bars, M., in press. Experimental and numerical study of mean zonal flows generated by librations of a rotating spherical cavity. Journal of Fluid Mechanics.

Spohn, T., Schubert, G., 2003. Oceans in the icy Galilean satellites of Jupiter? Icarus 161 (2), 456–467.

Tilgner, A., 1999. Driven inertial oscillations in spherical shells. Physical Review E 59 (2), 1789–1794.

Van Hoolst, T.V., Rambaux, N., Karatekin, O., Dehant, V., Rivoldini, A., 2008. The librations, shape and icy shell of Europa. Icarus 195 (1), 386–399.

Williams, J.G., Boggs, D.H., Yoder, C.F., Ratcliff, J.T., Dickey, J.O., 2001. Lunar rotational dissipation in solid body and molten core. Journal of Geophysical Research-Planets 106 (E11), 27933–27968.

Williams, J.P., Aharonson, O., Nimmo, F., 2007. Powering mercury's dynamo. Geophysical Research Letters 34 (21).

Wu, X., Bender, P.L., Peale, S.J., Rosborough, G.W., Vincent, M.A., 1997. Determination of mercury's 88 day libration and fluid core size from orbit. Planetary and Space Science 45 (1), 15–19.

Yoder, C.F., 1995. Venus' free obliquity. Icarus 117 (2), 250–286.